Kinematically complete study of low-energy electron-impact ionization of neon: Internormalized cross sections in three-dimensional kinematics

Xueguang Ren, Sadek Amami, Oleg Zatsarinny, Thomas Pflüger, Marvin Weyland, Woon Yong Baek, Hans Rabus, Klaus Bartschat, Don Madison, and Alexander Dorn

Phys. Rev. A **91**, 032707 — Published 18 March 2015

DOI: 10.1103/PhysRevA.91.032707

Kinematically complete study of low-energy electron-impact ionization of neon: Internormalized cross sections in 3D kinematics

Xueguang Ren,[1,2,*] Sadek Amami,[3] Oleg Zatsarinny,[4] Thomas Pflüger,[1,2] Marvin Weyland,[1,2] Woon Yoon Baek,[1] Hans Rabus,[1] Klaus Bartschat,[4] Don Madison,[3] and Alexander Dorn[2]

[1]*Physikalisch-Technische Bundesanstalt, 38116 Braunschweig, Germany*

[2]*Max-Planck-Institut für Kernphysik, 69117 Heidelberg, Germany*

[3]*Physics Department, Missouri University of Science and Technology, Rolla, Missouri 65409, USA*

[4]*Department of Physics and Astronomy, Drake University, Des Moines, Iowa 50311, USA*

(Dated: March 2, 2015)

Abstract

Low-energy (E_0 = 65 eV) electron-impact single ionization of Ne ($2p$) has been investigated to thoroughly test state-of-the-art theoretical approaches. The experimental data were measured using a reaction microscope, which can cover nearly the entire 4π solid angle for the secondary electron emission energies ranging from 2 eV to 8 eV, and projectile scattering angles ranging from 8.5° to 20.0°. The experimental triple-differential cross sections are internormalized across all measured scattering angles and ejected energies. The experimental data are compared to predictions from a hybrid second-order distorted-wave Born plus R-matrix approach, the distorted-wave Born approximation with inclusion of post-collision interaction (PCI), a three-body distorted-wave approach (3DW), and a B-spline R-matrix (BSR) with pseudostates approach. Excellent agreement is found between experiment and predictions from the 3DW and BSR models, for both the angular dependence and the relative magnitude of the cross sections in the full three-dimensional parameter space. The importance of PCI effects is clearly visible in this low-energy electron-impact ionization process.

PACS numbers: 34.80.Dp

* E-mail: ren@mpi-hd.mpg.de

I. INTRODUCTION

Electron-impact ionization of atoms and molecules is of fundamental importance in a wide variety of sciences and modeling applications, including the physics and chemistry of planetary atmospheres, reactive plasmas, and more recently [1–3] even radiation tumor therapy, in which the secondary low-energy electrons produced by primary ionizing radiation can effectively induce substantial strand breaks in deoxyribonucleic acid (DNA) and their subunits. Precise experimental data are hence important to aid in the development of theoretical models and to understand the mechanism of the ionization dynamics.

The full information about the ionization dynamics can be obtained in kinematically complete experiments, or so-called (e, 2e) studies [4, 5], which determine the momentum vectors of all free particles. Such experiments serve as a powerful tool to comprehensively test theoretical models that account for the quantum mechanical few-body interactions. In recent years, theory has made tremendous progress in describing the electron-impact ionization dynamics, which is now considered to be well understood for the simplest systems such as atomic hydrogen and helium [6–8].

Much more challenging, however, is the treatment of more complex targets, e.g., the neon ($2p$) and argon ($3p$) ionization dynamics. Theoretical models, which have been frequently used to describe ionization processes in heavy complex targets, are a hybrid distorted-wave Born approximation (DWBA) plus R-matrix (close-coupling) approach [9–12], the DWBA with inclusion of the post-collision interaction (PCI) by the Gamow factor calculated with the Ward-Macek method [13], the three-body distorted-wave (3DW) approach (see e.g. [14–20]), and most recently the B-spline R-matrix (BSR) approach [21, 22]. Except for BSR, which includes a large number of pseudostates to estimate the effect of the high-lying Rydberg

states and the ionization continuum in the *ab initio* solution of the close-coupling equations, the approaches treat at least some part of the process perturbatively to first or second order. The theoretical models have been tested by experiments over a wide range of impact energies, collision dynamics, and targets. Reasonable agreement between theoretical predictions and experimental findings has been found for high and sometimes also intermediate and low impact energies. (See, for example, [14–19, 21–29].)

Recent studies for the electron-impact ionization of Ne ($2p$) at an incident energy $E_0 =$ 100 eV showed an unprecedented agreement between experiment and BSR predictions regarding both the shape (i.e., the angular dependence) and the relative magnitude of the triple-differential cross sections (TDCS) [22]. The experiment was performed by measuring internormalized TDCS in the full three-dimensional (3D) parameter space, i.e., not limited to the most popular co-planar or other specialized geometries. These "3D-TDCS" presentations provide a thorough test ground for theory [22]. Since the physical effects of PCI as well as electron exchange and charge-cloud polarization in the projectile-target interaction are expected to become even more pronounced with decreasing projectile energy, the present study extends the previous work on electron-impact ionization of Ne ($2p$) to the even lower impact energy of $E_0 = 65$ eV to further test the different theories.

The TDCSs were measured by covering a large part of the full solid angle for the emitted electron. Since the experimental data are internormalized for different kinematical situations, a *single common scaling factor is sufficient* to fix the relative magnitude of the experimental and theoretical data for all cases. After deciding on that factor, the angular dependence and the relative magnitude of the measured TDCS can be compared with the theoretical predictions. The measurements reported here cover a range of ejected-electron energies ($E_2 = 2.0$ eV, 4.5 eV and 8.0 eV) and projectile scattering angles ($\theta_2 = 8.5°$, 12.5°,

and 20.0°). The experimental data are compared with theoretical predictions from several calculations based on the hybrid second-order DWBA plus R-matrix approach (DWB2-RM), the DWBA with inclusion of PCI using the Ward-Macek method (DWBA-WM) [13], 3DW, and BSR.

This paper is organized as follows. After a brief description of the experimental apparatus in Sect. II, we summarize the essential points of the four theoretical models in Sect. III. The results are presented and discussed in Sect. IV, before we finish with the conclusions. Unless specified otherwise, atomic units (a.u.) are used throughout.

II. EXPERIMENT

The experiment was performed with an advanced reaction microscope, which was especially built for the electron-impact experiment [30]. It was recently updated by using a newly developed pulsed photoemission electron gun and a pulsed electric field for fragment-ion detection [31]. Since details of the experimental setup can be found in [31, 32], only a brief outline will be given here. A well-focused ($\approx$ 1 mm diameter), pulsed electron beam crosses a supersonic neon gas jet, which is produced by supersonic gas expansion through a 30 µm nozzle and two-stage differential pumping. The pulsed electron beam is generated by a photoemission electron gun, in which a pulsed ultraviolet laser (266 nm) illuminates a tantalum photocathode (ΔT $\approx$ 0.5 ns and $\Delta E_0 \approx$ 0.5 eV).

Using uniform electric and magnetic fields, the fragments in the final state are projected onto two position- and time-sensitive multi-hit detectors equipped with fast delay-line read-out. For single ionization, triple coincidences of both outgoing electrons (e_1 and e_2) and the recoil ion are recorded. From the positions of the hits and the times of flight (TOF), the vector momenta of the detected particles can be determined. Note that the projectile

beam axis (defining the z-direction) is adjusted exactly parallel to the electric and magnetic extraction fields. Therefore, after passing the target gas jet, the beam arrives at the center of the electron detector, where a central bore in the multichannel plates allows for the undeflected electrons to pass without inducing a hit. The detection solid angle for electrons is close to 4π, apart from the acceptance holes at small forward and backward angles where the electrons end up in the detector bore.

III. THEORETICAL MODELS

We have used four different theoretical models to describe the present electron-impact ionization process. Their essential ingredients will be summarized below. More information can be found in the references given.

A. DWB2-RM

The hybrid approach is originally based on the work of Bartschat and Burke [9]. The key idea is the assumption that a "fast" projectile acts as a perturbation on the initial target, ultimately resulting in an ejected electron scattering from the residual ion. In this respect, it is a generalization of the photoelectron process, except that the Coulomb interaction between the projectile and the target leads to a number of terms in the multipole expansion, compared to a single term in the electric dipole approximation. Also, the projectile (described by a distorted wave) can interact with the target multiple times. In our model, we include second-order interactions, thereby labeling the first part of the model "DWB2". More details can be found in [10–12].

The second part of the model requires a description of the initial state and the scattering

of the ejected electron from the residual ion. For this part, we employ the R-matrix (RM) method to solve the resulting close-coupling equations. Since the computer code is limited to the use of a single set of orthogonal one-electron orbitals, we employ the multi-configuration expansions developed by Burke and Taylor [33] for the $(2s^2 2p^5)^2P$ and $(2s2p^6)^2S$ states of Ne^+ included in this part of the problem.

Until the development of the fully nonperturbative BSR with pseudostates approach described in the next subsection, DWB2-RM was the standard method to account at least partially for channel-coupling effects in electron-impact ionization of complex targets, i.e., beyond quasi-one and quasi-two electron systems. The major shortfalls of the method are the asymmetric treatment of the two electrons (one by a distorted wave, one by a close-coupling expansion) and the neglect of both exchange and PCI effects. Hence, we generally expect the method to be appropriate for incident energies of several hundred eV, highly asymmetry energy sharing, and small scattering angles of the (fast) projectile. However, even in situations like those investigated in the present work, we find that comparing with results from a well-tested model such as DWB2-RM remains useful, in light of the very complex BSR calculations. Such a comparison may also be helpful to check possible normalization issues that have been noticed to affect results obtained, for example, in models that use the correct asymptotic form of the three-body Coulomb problem but may not be sufficiently accurate for describing the actual ionization process near the nucleus. Given its ability to employ accurate representations of the initial bound state as well as the final ionic states and to account for the most important channel-coupling effects, DWB2-RM should be fairly reliable to predict the probability for the actual ionization process, although it may not predict the bending of the binary and recoil lobes (see below) according to PCI effects.

B. BSR

The details of the BSR calculations carried out for this work were described in [21, 22]. Briefly, we employ a 679-state nonrelativistic BSR (close-coupling) model, with 55 states representing the bound spectrum and the remaining 624 the target continuum. All singlet and triplet target states with total electronic angular momentum $L = 0 - 4$ were included. The continuum pseudostates in the present calculations cover the energy region up to 85 eV.

The R-matrix radius was set to $30\,a_0$, where $a_0 = 0.529 \times 10^{-10}$ m is the Bohr radius. We employed 70 B-splines to span this radial range using a semi-exponential knot grid. The scattering model contained up to 2,280 scattering channels, leading to generalized eigenvalue problems with matrix dimensions up to 150,000 in the B-spline basis that is used for the expansion of the outer target orbitals (including the pseudoorbitals) as well as the projectile wave function inside the R-matrix box. Partial waves for total orbital angular momenta $L \leq 25$ were obtained numerically, followed by a top-up procedure to estimate the contributions from even higher L values.

The ionization amplitudes were determined by a two-step process, in which the scattering amplitudes for excitation of the pseudostates are mapped to true continuum states of the ejected-electron–residual-ion system through overlap factors between the pseudostates and these continuum states. This projection method (details can be found in [34, 35]) corresponds to an effective interpolation scheme [36] that becomes increasingly accurate with increasing density of the pseudospectrum. To obtain numerically stable results, it is important to use the same close-coupling expansion (here just a two-state model with the $(2s^2 2p^5)^2P$ and $(2s2p^6)^2S$ states of Ne^+) to generate both the pseudostates in a bound-state close-coupling model and the physical electron-ion scattering states used for the projection. Since the

BSR approach, in contrast to the DWB2-RM model described above, employs individually optimized, and hence nonorthogonal, orbital sets, the two ionic states can be represented sufficiently well without relying on additional pseudoorbitals.

C. The Three-Body Distorted-Wave Approximation

The three-body distorted-wave (3DW) approach has been previously discussed in [19, 20, 27]. Here we present a brief overview with the key features of the theory necessary for the present discussion. In the present paper, two different approximations will be presented.

1. 3DW

In the 3DW model, the direct T-matrix is given by

$$T_{dir}^{3DW} = \langle \Psi_f | W | \Psi_i \rangle, \tag{1}$$

where, for ionization of an atom, the initial-state wave function Ψ_i is described as a product of the initial Hartree-Fock bound-state wave function $\psi_{\rm HF}$ for the target and a distorted-wave function χ_i for the incoming electron (the projectile):

$$\Psi_i = \psi_{\rm HF}\, \chi_i. \tag{2}$$

The perturbation (W) is given by

$$W = V_i - U_i. \tag{3}$$

Here V_i is the interaction between the incident electron and the atom, and U_i is the initial-state spherically symmetric static approximation for U_i, which is asymptotically equal to zero. The final-state wave function is described as a product of two final-state continuum

electron distorted waves (χ_1 for the scattered and χ_2 for the ejected electron, respectively), and the Coulomb interaction between the outgoing electrons (C_{12}), normally called the PCI:

$$\Psi_f = \chi_1\ \chi_2\ C_{12}. \tag{4}$$

In the 3DW model, we use the exact electron-electron Coulomb interaction between the two electrons for C_{12}, which requires the evaluation of a six-dimensional (6D) numerical integral. This factor is a product of a gamma factor and a hypergeometric function:

$$\begin{aligned} &C_{12}(\boldsymbol{r}_{12}, \boldsymbol{k}_{12}) \\ &\quad = e^{-\frac{\pi\gamma}{2}}\,\Gamma(1-i\gamma)\,{}_1F_1(i\gamma, 1, -i[k_{12}r_{12} + \boldsymbol{k}_{12}\cdot\boldsymbol{r}_{12}]). \end{aligned} \tag{5}$$

Here $\boldsymbol{r}_{12}$ is the relative distance between the two electrons, $\boldsymbol{k}_{12}$ is the relative momentum, $\boldsymbol{k}_{12} = \mu\boldsymbol{\nu}_{12}$, $\mu = \frac{1}{2}$ in atomic units is the reduced mass for the two continuum electrons, and $\boldsymbol{\nu}_{12}$ is the relative velocity between the two electrons. The factor ${}_1F_1$ is a confluent hypergeometric function, $\Gamma(1-i\gamma)$ is the gamma function, and $\gamma = \frac{1}{\nu_{12}}$ is the Sommerfeld parameter, which is a measure of the strength of the Coulomb interaction between the two electrons.

Finally, the direct 3DW T-matrix becomes

$$T_{dir}^{3DW} = \langle \chi_1\,\chi_2\,C_{12}|V_i - U_i|\psi_{\rm HF}\,\chi_i\rangle, \tag{6}$$

The exchange T-matrix T_{exc}^{3DW} is identical to Eq. (6), except that the scattered and ejected electrons are exchanged in the final-state wave function Ψ_f.

2. DWBA-WM

The second approximation we will present is the DWBA-WM (Distorted Wave Born Approximation with Ward-Macek method) to calculate the TDCS for ionization of Ne ($2p$) [13].

In this model, the term $\boldsymbol{k}_{12} \cdot \boldsymbol{r}_{12}$ is replaced by $k_{12} r_{12}^{ave}$, where the average value r_{12}^{ave} of the electron-electron separation is defined by

$$r_{12}^{ave} = \frac{\pi^2}{16\varepsilon_t}\left(1 + \frac{0.627}{\pi}\sqrt{\varepsilon_t}\ln\varepsilon_t\right)^2, \tag{7}$$

with ε_t denoting the total energy of the two electrons. Since the Ward-Macek approximation for the Coulomb repulsion factor C_{12}^{WM} does not explicitly depend on the electronic coordinates, it can be removed from the T-matrix integral. This reduces the computational difficulty and required time substantially.

We can write the square of the Coulomb factor as

$$|C_{12}^{\mathrm{WM}}|^2 = N_{ee}\,|{}_1F_1(i\gamma, 1, -2ik_{12}r_{12}^{ave})|^2, \tag{8}$$

where N_{ee}, the so-called Gamov factor [13], is defined as

$$N_{ee} = |e^{-\frac{\pi\gamma}{2}}\Gamma(1 - i\gamma)|^2 = \frac{\pi/k_{12}}{(e^{\pi/k_{12}} - 1)}. \tag{9}$$

With these approximations, the direct DWBA-WM T-matrix becomes

$$T_{dir}^{DWBA\text{-WM}} = C_{12}^{\mathrm{WM}}[\langle\chi_1\,\chi_2|V_i - U_i|\psi_{\mathrm{HF}}\,\chi_i\rangle], \tag{10}$$

or

$$T_{dir}^{DWBA\text{-WM}} = C_{12}^{\mathrm{WM}}\,T_{dir}^{DWBA}, \tag{11}$$

Finally, with the T-matrix given in atomic units, the TDCS in both theories can be expressed as

$$TDCS = \frac{1}{(2\pi)^5}\frac{k_1 k_2}{k_i}\left(|T_{dir}|^2 + |T_{exc}|^2 + |T_{dir} - T_{exc}|^2\right), \tag{12}$$

where k_i, k_1, and k_2 are the magnitudes of the momenta of the initial, scattered, and ejected electrons, respectively.

Calculations are typically classified in terms of orders of perturbation theory. However, this classification can become ambiguous since any physics contained in the approximate wave function is contained to all orders of perturbation theory, while the physics contained in the perturbation will be contained to the order of the calculation. For the 3DW model, the electron-electron interaction is contained in the approximate final-state wave function; hence, this physics is contained to all orders of perturbation theory. The non-perturbative BSR calculation also accounts for PCI to all orders of perturbation theory, but only within the R-matrix box. This is the reason, why in the BSR calculations for ionization the box size is generally chosen larger than required by the typical rule that exchange between the projectile electron and the target electrons is negligible. The DWBA-WM model contains an estimate for the electron-electron interaction in the approximate system wave function, i.e., it contains an approximation for PCI to all orders. The DWB2-RM model, finally, contains the electron-electron interaction in the perturbation, but only inside the reaction region, i.e., a standard (small) R-matrix box of about 12 a_0 in the present case. Within this box, PCI would be accounted for to second order, but this is not the region where it is most important. Hence, DWB2-RM neglects almost all PCI effects.

IV. RESULTS AND DISCUSSION

Figure 1 exhibits the experimental and theoretical TDCSs for ionization of Ne ($2p$) by 65 eV electron-impact as three-dimensional (3D) polar plots for a projectile scattering angle of $\theta_1 = -12.5^\circ$ as a function of the emission direction of a slow ejected electron with $E_2 =$ 2.0 eV energy. Panel 1 (a) corresponds to the experimental data, while panels 1 (b)$-$(e) show the calculated results from the BSR, DWB2-RM, 3DW and DWBA-WM models, respectively. The projectile enters from the bottom and is scattered to the left (hence the

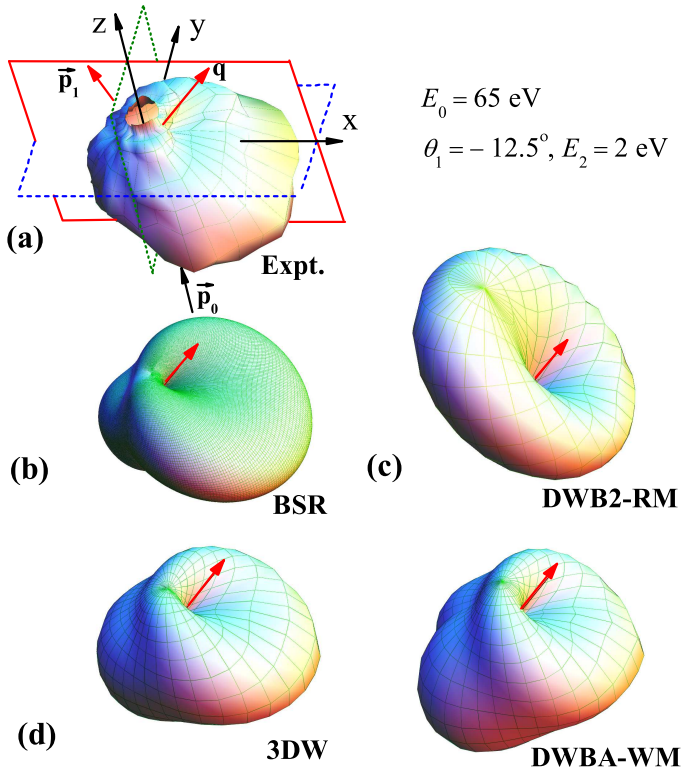

FIG. 1. (Color online): Experimental and theoretical TDCS for ionization of Ne ($2p$) by incident electrons with energy $E_0 = 65$ eV, presented as 3D images. The scattering angle is $\theta_1 = -12.5^\circ \pm 2.5^\circ$, and the ejected electron energy is $E_2 = 2.0$ eV ± 1.0 eV. Panel (a) shows the experimental 3D TDCS, while panels (b)−(e) represent the predictions from the BSR, DWB2-RM, 3DW, and DWBA-WM models, respectively.

minus in the notation for the angle). These two vectors define the scattering (xz) plane as indicated by the solid frame in panel (a). The momentum transfer to the target is indicated by the arrow labeled $\boldsymbol{q}$.

In these 3D-plots, the TDCS for a particular direction is given as the distance from the origin of the plot to the point on the surface, which is intersected by the ionized electron's emission direction. [Below we follow the common notation of referring to the slower of the two outgoing electrons as "ionized", "emitted", or "ejected", and to the faster one

as "scattered".] The kinematics chosen displays exemplarily the principal features of the emission pattern: it is governed by the well-known binary and recoil lobes. The binary lobe is oriented roughly along the direction of the momentum transfer $\boldsymbol{q}$, thus corresponding to electrons emitted after a single binary collision with the projectile. In the opposite direction the recoil lobe is found, where the outgoing slow electron additionally backscatters in the ionic potential. For ionization of p-states, the binary peak often exhibits a minimum along the momentum transfer direction. This is the result of the characteristic momentum profile of a p-orbital that has a node for vanishing momentum. Additionally, the emitted electron is repelled by the scattered projectile due to the long-range nature of the Coulomb force. These PCI effects tilt the binary and recoil lobes away from the scattered projectile direction. Further, the binary lobe exhibits a much flatter shape in comparison with 3D emission patterns for high and intermediate energies.

Comparing the experimental results to the various theoretical predictions, we see that the BSR and 3DW calculations generally show good agreement with the data. The DWBA-WM calculation yields reasonable agreement with the experimental data in the binary region, but significant discrepancies appear in the recoil region, particularly for the cross sections outside the scattering plane. The DWB2-RM calculations often also reproduces the relative shape of the experimental 3D cross sections, except that major discrepancies are observed near the direction of the scattered projectile. This problem is due to the fact that PCI effects are effectively neglected in the DWB2-RM model while they are accounted for to all orders in the 3DW, to all orders in the BSR (up to 30 a_0 away from the center), and approximately (everywhere) to all orders in DWBA-WM.

For a more quantitative comparison between experiment and theory, cross section cuts through the 3D TDCS image along the three orthogonal planes as indicated in Fig. 1 (a) are

presented in Figs. 2−4. Those are the xz-plane or scattering plane (solid line in Fig. 1(a)), the yz-plane or perpendicular plane (dotted line), and the xy-plane or full-perpendicular plane (dashed line), in Figs. 2−4 these planes are shown in the left, middle, and right columns of the figures, respectively. In Figs. 2, 3 and 4 the same experimental data are compared to the BSR and DWB2-RM results (Fig. 2), the 3DW and DWBA-WM results (Fig. 3) and the BSR and 3DW calculations (Fig. 4), respectively. The studied kinematical conditions correspond to projectile scattering angles from $\theta_1 = -8.5°$ to $-20°$ and ejected electron energies from $E_2 = 2.0$ eV to 8.0 eV. The global scaling factor used to normalize the experimental data to the theories was found by achieving the best visual fit of experiment and the BSR and 3DW calculations for the TDCS in the scattering plane at $\theta_1 = -12.5°$ and $E_2 = 2.0$ eV, as shown in Fig. 2 (d) and Fig. 3 (d). It was subsequently applied to all other kinematics and planes.

In Figs. 2−4 the experimental cross sections are presented as a function of the ejected electron emission angles. The data are integrated over an out-of-plane angular range of ± 10°. This should have only minor implications for the scattering plane, where the cross section varies slowly for small out-of-plane angles. The scattering plane cuts through the binary and the recoil peaks, and it contains the momentum transfer vector indicated in the diagrams by an arrow. In the scattering plane, we observe the well-known binary and recoil patterns. The characteristic dip along the $\boldsymbol{q}$ direction or splitting of the binary peak mentioned above is indicated in the experimental data in particular for the larger scattering angle case $\theta_1 = -20°$. Here, one smaller peak close to the projectile scattering (i.e., near-forward) direction and one larger peak at larger angles with respect to $\boldsymbol{q}$ are observed. This is another signature of the enhanced PCI effect in the low-energy regime, where the binary peak is significantly suppressed near the forward direction.

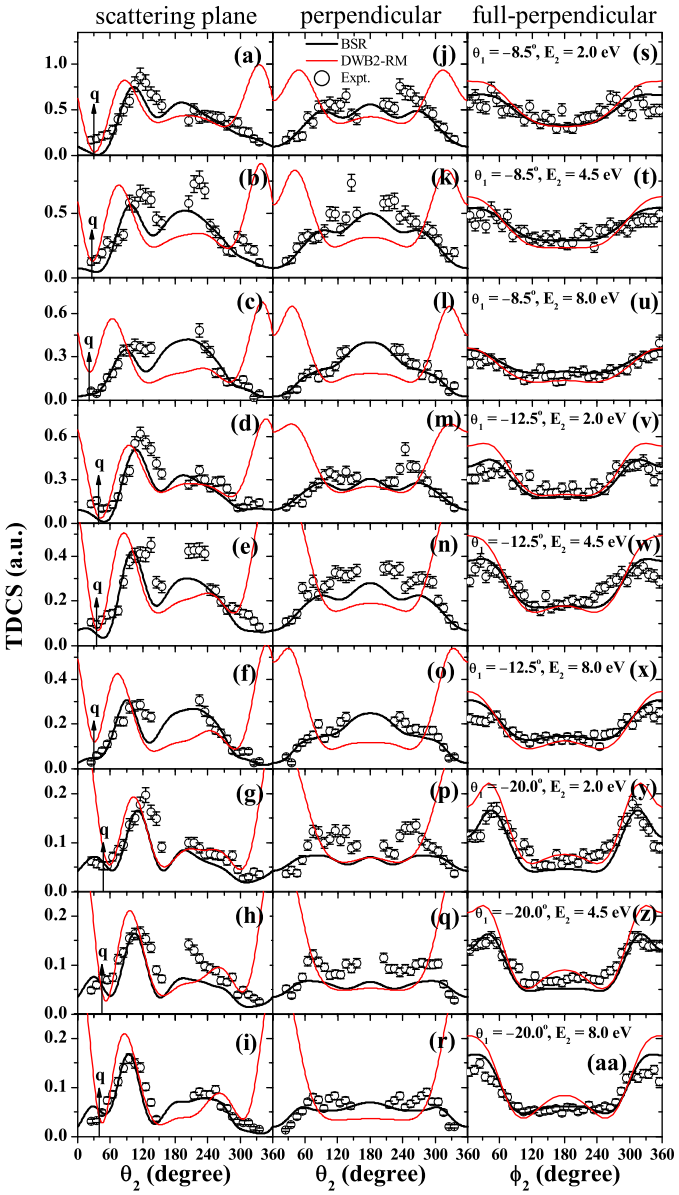

FIG. 2. (Color online): TDCS for the ionization of Ne ($2p$) presented as a function of the ejected electron (e_2) emission angle at different scattering angles θ_1 ($-8.5^\circ \pm 1.5^\circ$, $-12.5^\circ \pm 2.5^\circ$, $-20^\circ \pm 5^\circ$) and ejected-electron energies E_2 (2.0 eV ± 1.0 eV, 4.5 eV ± 1.5 eV, 8.0 eV ± 2.0 eV). Left column: TDCS in the xz-plane (scattering plane). Central column: TDCS in the yz-plane (perpendicular plane). Right column: TDCS in the xy-plane (full-perpendicular plane). The various collision kinematics (θ_1, E_2) are labeled in the panels of the right column. Thick black lines: BSR model, thin red lines: DWB2-RM model. The open circles (○) with error bars represent the experimental data.

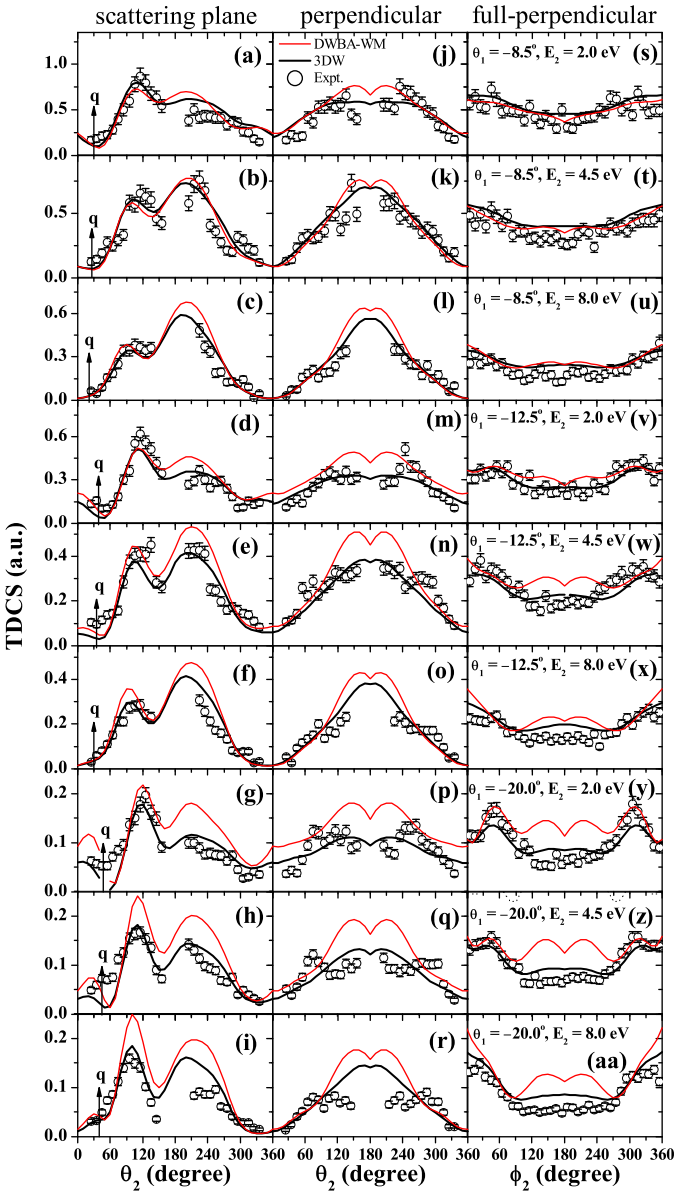

FIG. 3. (Color online): Same as Fig. 2, except that the theoretical calculations are the 3DW (thick black lines) and DWBA-WM (thin red lines).

In the perpendicular plane, there is an indication of a three-lobe structure, particularly for the larger projectile scattering angles. This plane cuts through the double-lobe binary peak, thereby resulting in two symmetric maxima in the ranges $\theta_2 = 60° - 90°$ and $\theta_2 = 270° - 300°$, respectively. In addition the recoil lobe gives rise to the central maximum at $\theta_2 = 180°$. In this plane PCI acts strongest for emission angles near 0° and 360°.

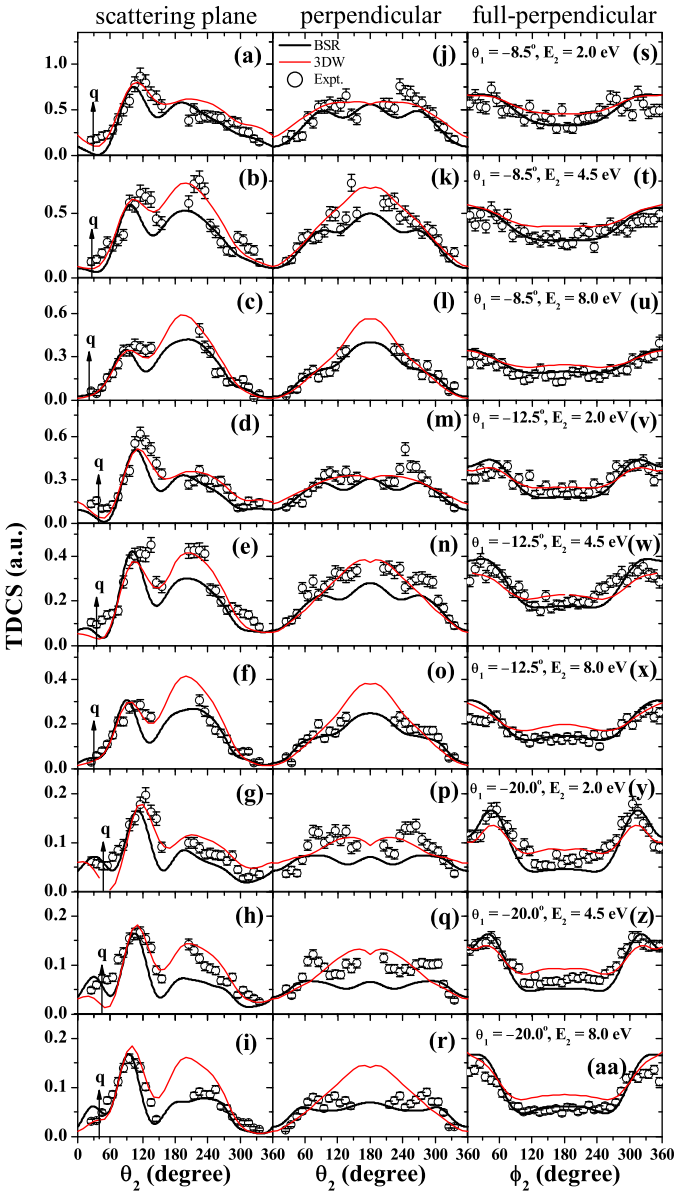

FIG. 4. (Color online): Same as Fig. 2, except that the theoretical calculations are the BSR (thick black lines) and 3DW (thin red lines).

In the full-perpendicular plane, which is perpendicular to the incident-projectile direction, the ejected electron's polar angle is fixed to $\theta_2 = 90°$ and the azimuthal angle ϕ_2 is varied. The observed structures for emission at azimuthal angles near 0° and 360° and also for some cases near $\phi_2 = 60°$ and 300° are caused by the binary peak. The recoil peak most likely influences the cross sections near $\phi_2 = 180°$. In this plane the influence of PCI appears to

be small over the entire angular range.

In Fig. 2 the experimental data are compared to predictions from the BSR and DWB2-RM models. Overall, excellent agreement between BSR and the experimental data is noticed regarding both the angular dependence of the cross sections and the relative magnitude over the entire range of angle and energy conditions analyzed. The general features observed in the three planar cuts, including the strong PCI effect near the forward direction, are well reproduced by the BSR theory, except that for some cases the experimental cross section exhibits enhanced intensity for the recoil peaks in the scattering plane, as seen in panels (b), (e), and (h) of Fig. 2. In the perpendicular plane, the BSR theory is able to reproduce the observed three-lobe structure, while slight deviations in the magnitude of the three-lobe structure are visible for the case of $\theta_1 = -20^\circ$ (c.f. panels (p)−(r) in Fig. 2). The best agreement between BSR and the experimental data is found for the full-perpendicular plane.

Regarding the DWB2-RM theory, significant discrepancies between its predictions and the experimental data are observed near the projectile forward direction, as can be seen in the left (scattering plane) and central columns (perpendicular plane) of Fig. 2. This problem is again due to the very weak PCI effect in this model. Outside the forward direction ($\theta_2 = 60^\circ - 300^\circ$) the DWB2-RM calculations often yield reasonable agreement with the experimental data and the BSR theory. In the full-perpendicular plane, good agreement is found between the DWB2-RM calculations and the measurements.

In Fig. 3 the experimental data are compared to predictions from the 3DW and DWBA-WM models. The DWBA-WM results are generally in good agreement with the experimental data, especially for the smallest projectile scattering angle of $\theta_1 = -8.5^\circ$. For the larger scattering angles of $\theta_1 = -12.5^\circ$ and -20°, DWBA-WM overestimates the magnitude of the recoil-peak contributions in all three planes. The DWBA-WM model provides a clear

improvement over the DWB2-RM calculations in that its predictions become reasonable in the angular range of θ_2 close to 0° and 360°. This indicates that the PCI effect plays a very important role in the low-energy ionization processes studied here.

There is overall excellent agreement between the 3DW predictions and the experimental data concerning both the angular dependence of the cross sections and the relative magnitude over the entire range of angle and energy conditions analyzed. This is particularly true in the scattering plane (left column of Fig. 3) and the full-perpendicular plane (right column of Fig. 3). The only noticeable systematic differences occur in the perpendicular plane (central column of Fig. 3), where the 3DW predicts less structure than is indicated in the data.

Overall, both the 3DW and BSR theories exhibit excellent agreement with the experimental data. A direct comparison between the experimental data and these two apparently best calculations is presented in Fig. 4. Noticeable deviations include some results for the scattering plane, where the BSR calculations slightly underestimate the magnitude of the recoil peaks for the ejected energy of $E_2 = 4.5$ eV compared to the experimental data and the 3DW calculations, and the case of $\theta_1 = -20.0°$ and $E_2 = 8.0$ eV, where the 3DW model overestimates the magnitude of the recoil peak. In the perpendicular plane, the BSR calculation predicts the structure seen in the data better than the 3DW. The best overall agreement between theory and the experiment is found for the cross sections in the full-perpendicular plane.

V. CONCLUSIONS

We have reported a comprehensive study of the electron-impact ionization dynamics of Ne $(2p)$ at a low incident projectile energy of 65 eV. The three-dimensional representations of the triple-differential cross sections obtained experimentally were internormalized across all

scattering angles of θ_1 from $-8.5°$ to $-20.0°$ and ejected electron energies of E_2 from 2.0 eV to 8.0 eV, thus providing a thorough test for the theoretical models. The experimental data were compared to predictions from the DWB2-RM, DWBA-WM, 3DW, and BSR models. The DWB2-RM model provides reasonable cross sections for ionization geometries of θ_2 from $60°$ to $300°$, where PCI effects do not play a significant role. The predictions from the DWBA-WM model, where PCI is accounted for via the Ward-Macek approximation, improves the results for θ_2 close to $0°$ and $360°$. This clearly indicates that PCI effects play a very important role in the present low-energy ionization processes.

The experimental data and the BSR and 3DW results, on the other hand, reveal an unprecedented degree of agreement not only in the angular dependence but also in the relative magnitude of the triple-differential cross section over a range of scattering angles and ejection energies in the entire 3D parameter space.

ACKNOWLEDGMENTS

This work was supported, in part, by the United States National Science Foundation under grants No. PHY-1068237 (SA and DM), No. PHY-1212450 and No. PHY-1430245 (OZ and KB), and the XSEDE allocations No. PHY-090031 (OZ and KB) and TG-MCA075029 (SA and DM). SA would also like to thank the Libyan Ministry of Higher Education's Scholarship for funding.

[1] B. Boudaïffa, P. Cloutier, D. Hunting, M. Huels, and L. Sanche, Science **287**, 1658 (2000).

[2] G. Hanel, B. Gstir, S. Denifl, P. Scheier, M. Probst, B. Farizon, M. Farizon, E. Illenberger, and T. D. Märk, Phys. Rev. Lett. **90**, 188104 (2003).

[3] S. Tonzani and C. H. Greene, J. Chem. Phys. **125**, 094504 (2006).

[4] H. Ehrhardt, M. Schulz, T. Tekaat, and K. Willmann, Phys. Rev. Lett. **22**, 89 (1969).

[5] U. Amaldi, A. Egidi, R. Marconero, and G. Pizzella, Rev. Sci. Instrum. **40**, 1001 (1969).

[6] T. N. Resigno, M. Baertschy, W. Isaacs, and C. McCurdy, Science **286**, 2474 (1999).

[7] X. Ren, I. Bray, D. V. Fursa, J. Colgan, M. Pindzola, T. Pflüger, A. Senftleben, S. Xu, A. Dorn, and J. Ullrich, Phys. Rev. A **83**, 052711 (2011).

[8] O. Zatsarinny and K. Bartschat, Phys. Rev. Lett. **107**, 023203 (2011).

[9] K. Bartschat and P. G. Burke, J. Phys. B **20**, 3191 (1987).

[10] R. H. G. Reid, K. Bartschat, and A. Raeker, J. Phys. B **31**, 563 (1998).

[11] Y. Fang and K. Bartschat, J. Phys. B **34**, L19 (2001).

[12] K. Bartschat and O. Vorov, Phys. Rev. A **72**, 022728 (2005).

[13] S. J. Ward and J. H. Macek, Phys. Rev. A **49**, 1049 (1994).

[14] A. Naja, E. M. S. Casagrande, A. Lahmam-Bennani, M. Stevenson, B. Lohmann, C. D. Cappello, K. Bartschat, A. Kheifets, I. Bray, and D. V. Fursa, J. Phys. B **41**, 085205 (2008).

[15] L. R. Hargreaves, M. Stevenson, and B. Lohmann, J. Phys. B **43**, 205202 (2010).

[16] M. A. Stevenson, L. R. Hargreaves, B. Lohmann, I. Bray, D. V. Fursa, K. Bartschat, and A. Kheifets, Phys. Rev. A **79**, 012709 (2009).

[17] X. Ren, A. Senftleben, T. Pflüger, A. Dorn, K. Bartschat, and J. Ullrich, Phys. Rev. A **83**, 052714 (2011).

[18] X. Ren, A. Senftleben, T. Pflüger, J. Ullrich, K. Bartschat, and A. Dorn, Phys. Rev. A **89**, 029904(E) (2014).

[19] S. Amami, M. Ulu, Z. N. Ozer, M. Yavuz, S. Kazgoz, M. Dogan, O. Zatsarinny, K. Bartschat, and D. Madison, Phys. Rev. A **90**, 012704 (2014).

[20] S. Amami, A. Murray, A. Stauffer, K. Nixon, G. Armstrong, J. Colgan, and D. Madison, Phys. Rev. A **90**, 062707 (2014).

[21] O. Zatsarinny and K. Bartschat, Phys. Rev. A **85**, 032708 (2012).

[22] T. Pflüger, O. Zatsarinny, K. Bartschat, A. Senftleben, X. Ren, J. Ullrich, and A. Dorn, Phys. Rev. Lett. **110**, 153202 (2013).

[23] H. Chaluvadi, C. G. Ning, and D. Madison, Phys. Rev. A **89**, 062712 (2014).

[24] O. Al-Hagan, C. Kaiser, A. J. Murray, and D. Madison, Nat Phys **5**, 59 (2009).

[25] O. Al-Hagan, A. J. Murray, C. Kaiser, J. Colgan, and D. H. Madison, Phys. Rev. A **81**, 030701 (2010).

[26] S. Bellm, J. Lower, R. P. McEachran, E. Weigold, C. Ryan-Anderson, and D. H. Madison, Phys. Rev. A **78**, 062707 (2008).

[27] D. H. Madison and O. Al-Hagan, Journal of Atomic, Molecular, and Optical Physics **2010**, 24 (2010).

[28] A. Senftleben, O. Al-Hagan, T. Pflger, X. Ren, D. Madison, A. Dorn, and J. Ullrich, The Journal of Chemical Physics **133**, 044302 (2010).

[29] K. L. Nixon, A. J. Murray, H. Chaluvadi, S. Amami, D. H. Madison, and C. Ning, The Journal of Chemical Physics **136**, 094302 (2012).

[30] X. Ren, A. Senftleben, T. Pflüger, A. Dorn, K. Bartschat, and J. Ullrich, J. Phys. B **43**, 035202 (2010).

[31] X. Ren, T. Pflüger, M. Weyland, W. Y. Baek, H. Rabus, J. Ullrich, and A. Dorn, J. Chem. Phys. **141**, 134314 (2014).

[32] J. Ullrich, R. Moshammer, A. Dorn, R. Dörner, L. Schmidt, and H. Schmidt-Böcking, Rep. Prog. Phys. **66**, 1463 (2003).

[33] P. G. Burke and K. T. Taylor, J. Phys. B **8**, 2620 (1975).

[34] O. Zatsarinny and K. Bartschat, Phys. Rev. A **85**, 062709 (2012).

[35] O. Zatsarinny and K. Bartschat, J. Phys. B **46**, 112001 (2013).

[36] I. Bray, C. J. Guilfoile, A. S. Kadyrov, D. V. Fursa, and A. T. Stelbovics, Phys. Rev. A **90**, 022710 (2014).